

A holistic approach to inversion of frequency-domain airborne EM data

Ross Brodie¹ and Malcolm Sambridge²

ABSTRACT

We have developed a holistic method for simultaneously calibrating, processing, and inverting frequency-domain airborne electromagnetic data. A spline-based, 3D, layered conductivity model covering the complete survey area was recovered through inversion of the entire raw airborne data set and available independent conductivity and interface-depth data. The holistic inversion formulation includes a mathematical model to account for systematic calibration errors such as incorrect gain and zero-level drift. By taking these elements into account in the inversion, the need to preprocess the airborne data prior to inversion is eliminated. Conventional processing schemes involve the sequential application of a number of calibration corrections, with data from each frequency treated separately. This is followed by inversion of each multifrequency sample in isolation from other samples.

By simultaneously considering all of the available information in a holistic inversion, we are able to exploit interfrequency and spatial-coherency characteristics of the data. The formulation ensures that the conductivity and calibration models are optimal with respect to the airborne data and prior information. Introduction of interfrequency inconsistency and multistage error propagation stemming from the sequential nature of conventional processing schemes is also avoided. We confirm that accurate conductivity and calibration parameter values are recovered from holistic inversion of synthetic data sets. We demonstrate that the results from holistic inversion of raw survey data are superior to the output of conventional 1D inversion of final processed data. In addition to the technical benefits, we expect that holistic inversion will reduce costs by avoiding the expensive calibration-processing-recalibration paradigm. Furthermore, savings may also be made because specific high-altitude zero-level observations, needed for conventional processing, may not be required.

INTRODUCTION

A variety of weaknesses have been noted in the standard calibration procedures applied to frequency-domain electromagnetic (FDEM) systems. Errors were noted by Fitterman (1998) in values derived for amplitude- and phase-calibration parameters from on-ground measurements. Similarly, errors in the quantification of the drift in the zero-level of each of the in-phase and quadrature data streams, as determined from measurements made during periodic excursions to high altitude within each flight are discussed by Deszcz-Pan et al. (1998) and Huang and Fraser (1999). Systematic calibration error is the term we use to describe the effect of incorrect values for calibration parameters that influence entire subsets of the data (e.g., a constant phase shift for a specific frequency on a particular day of flying).

Conventional data processing includes subtraction of the high-altitude zero levels, filtering to remove short period noise (e.g., power line noise), and leveling. Leveling is primarily guided by the aim of generating coherent apparent conductivity maps that are free of features that the processor interprets to be indicative of the presence of residual error. Such artifacts are typically those features correlated with a particular acquisition entity (e.g., a flight). Because leveling is carried out independently for each frequency, it is impossible to identify and correct any interfrequency inconsistencies that may exist or to ensure that additional inconsistencies are not introduced.

Identification of the features that are considered to be artifacts is an inherently subjective process. Having selected a feature, the processor must choose which of several possible parameter classes to correct (e.g., gain, phase, and bias). Because of the complex nonlinear relationship between the calibration parameters and the in-phase and quadrature data and thence the apparent conductivity, it is un-

Manuscript received by the Editor November 8, 2005; revised manuscript received March 28, 2006; published online October 18, 2006.

¹Australian National University, Research School of Earth Sciences, Mills Road, Canberra ACT 0200, Australia and Geoscience Australia. E-mail: ross.c.brodie@ga.gov.au.

²Australian National University, Research School of Earth Sciences, Mills Road, Canberra ACT 0200, Australia. E-mail: malcolm.sambridge@anu.edu.au.

© 2006 Society of Exploration Geophysicists. All rights reserved.

likely that even an experienced processor can choose the correct combination of parameters and adjustments. Although a degree of optimization may be achieved through several time-consuming, sequentially applied correction iterations (Valleau, 2000), the final result is far from the best that might result from a more objective and systematic approach. Furthermore, sequentially applied corrections allow the propagation of errors from one processing step to the next. Huang and Fraser (1999) have noted that poor leveling decisions may generate false features and eliminate real features.

Coherent and artifact-free apparent conductivity maps are a reasonable, but insufficient, criterion for a good outcome. We suggest that a better criterion would be that the processed data from all frequencies be consistent with a single 3D conductivity model, and moreover, that the model be consistent with prior independent information. It is not surprising, then, that inversion of processed data generally reveals inconsistencies between the data and prior information and that it is impossible to reduce data misfits to expected levels, even when adequate model complexity is allowed for (Deszcz-Pan et al., 1998; Brodie et al., 2004b).

Airborne electromagnetic data exhibit a degree of consistency that depends on the subsurface conductivity distribution, the physics of the acquisition system and the sampling pattern of the survey. Because conventional 1D inversion methods (e.g., Huang and Fraser, 2003; Farquharson et al., 2004) treat each airborne sample independently, they fail to capitalize on the spatial coherency in the data.

Here we present a new approach to address these issues. We call it a holistic approach because the overall notion is to simultaneously calibrate, process and invert the data. We briefly discuss related work and provide an example of systematic calibration error resulting from conventional approaches, which is used later for comparison with the holistic inversion results. The holistic approach was first outlined by Brodie and Sambridge (2004); here it is formally described and then demonstrated with synthetic and real survey data examples. We conclude that the holistic approach produces superior results compared to conventional techniques, reduces the subjectivity of data processing decisions, and provides potential cost savings.

Related work

Deszcz-Pan et al. (1998) introduce the calibration model concept. They invert for gain, phase, and bias correction factors using auxiliary ground geophysical data and a subset of the adjacent airborne data. They then applied the correction factors and proceeded with conventional 1D inversion. A similar regression method is used by Brodie et al. (2004a) to derive gain-correction factors. In the holistic approach, we adopt the calibration model idea but simultaneously invert for calibration and conductivity model parameters using the entire airborne data rather than just those samples adjacent to auxiliary ground geophysical data.

Huang and Fraser (1999) propose an automated leveling technique based on pseudotie-lines and nonlinear filters. Green (2003) describes an inversion-based bias correction method that minimizes the data differences between adjacent lines. Ley-Cooper and Macnae (2004) suggests an empirical recalibration method for gain correction based on the expected characteristics in a transformed data domain.

To take advantage of spatial coherency in the data, Gyulai and Ormos (1999) use a laterally continuous 2D conductivity model, parameterized by sine- and cosine-basis functions, for the inversion of resistivity data. Auken et al. (2005) simultaneously inverted resistiv-

ity data along a profile to estimate a conductivity model parameterized by discrete 1D models connected laterally along the profile via roughness constraints. Profile-based airborne FDEM data are considered by Sasaki (2004), who uses a similarly parameterized conductivity model and also inverted for flight-height parameters.

Systematic calibration error example

Systems that can be calibrated at high altitude using internal calibration coils have been developed (Hodges, 2002). Such systems are an advance on ground-calibrated systems; however, they are still affected by temporal changes and rely on the accuracy of the initial calibration of the internal coils and their stability. The RESOLVE system is one that can be calibrated at high altitude using internal calibration coils.

We use RESOLVE data to demonstrate the effect of systematic calibration error here and for the examples of the application of the holistic inversion to synthetic and real data, later in the paper. The data were acquired during 2002 over the Riverland area in South Australia. In this survey, the system was configured with six coil sets operating at the frequencies 385, 1518, 3323, 6135, 25,380, and 106,140 Hz. The transmitter-receiver separation was 7.86 m for the five horizontal, coplanar coil sets and 8.99 m for the single vertical-coaxial (3323 Hz) coil set. The survey was flown with a nominal bird height of 30 m along north-south flight lines spaced mainly at 150 m but at 300 m in part of the area. East-west tie lines were flown at approximately 6 km spacing. The data were processed in the conventional manner by the survey contractor. The noise model of Green and Lane (2003) was used to estimate noise in the airborne data.

The conventionally processed data were inverted using the 1D sample-by-sample inversion algorithm described by Brodie et al. (2004b). They found that the inversion could not find any plausible five-layer model that fit the data adequately and that the data were inconsistent with downhole conductivity logs. To fit these data to plausible layered conductivity models, it was necessary to scale the data by factors derived from a regression of the data against forward models of the downhole log data (Brodie et al., 2004a).

Figure 1a shows the layer 2 thickness image resulting from the five-layer 1D sample-by-sample inversion of the conventionally calibrated and processed data before any scaling factors had been applied. Figure 1b shows the 106,140-Hz in-phase inversion residuals normalized by the estimated noise in the 106,140-Hz in-phase data (quantities of this type will be referred to as noise-normalized residuals). It is clear that there are numerous artifacts coincident with the north-south flight lines in the thickness image. The noise-normalized residuals are large and are spatially correlated with individual flights and lines. Together, these characteristics suggest some form of residual or introduced systematic error.

The inset in Figure 1b shows pseudolayer half-space apparent depths derived from the data in conjunction with the apparent conductivities (Fraser, 1978). Because the patterns observed in the apparent depth data are similar to those in the noise-normalized residuals, we are confident that these features are not just caused by a shortcoming of our conventional 1D inversion. It is expected that both the apparent depth and apparent conductivity data should exhibit a similar degree of coherency. In this case, we suspect that systematic error

was present in the processed in-phase and quadrature data and that a smooth apparent conductivity was produced by attributing all errors to the apparent depth data.

METHOD

Conductivity model

For the geophysical application of immediate interest to us, salinity mapping in sedimentary environments, we consider the subsurface to be comprised of N discrete layers stacked in layer-cake fashion. The natural logarithm of the layer conductivities and thicknesses are parameterized with bicubic B-spline surfaces (Bartels et al., 1987). The thickness and conductivity of each of the layers varies laterally and continuously. However, at any particular horizontal location, the conductivity of any given layer is constant from the top to the bottom of the layer. The bottom layer is assumed to be infinitely thick. Each spline surface is defined by a mosaic of surface patches that form a mesh as shown in Figure 2. A control vertex, or spline node, lies at each mesh intersection and is assigned a corresponding spline node coefficient. The node locations are chosen at the beginning of the procedure and remain fixed throughout.

The B-spline parameterization allows us to choose a node spacing so that the subsurface conductivity can be represented adequately with as few model parameters as possible. The node spacing is dependent on the minimum of the expected scale length of lateral conductivity variations, and the airborne system’s footprint (Liu and Becker, 1990). B-splines are smooth, locally supported, continuous basis functions, which we feel are particularly suitable given the local-averaging effect of the footprint. Other classes of basis function are also possible, e.g., constant blocks, linear or bilinear, all of which could be used equally well in a holistic inversion.

An N -layered conductivity model can be completely defined by $2N - 1$ (N conductivity and $N - 1$ thickness) spline meshes. The value of the spline surface at any point x, y that lies on the i th row and j th column of patches of the k th mesh is denoted $B_{ijk}(x, y)$. It is evaluated through the weighted sum of the 16 adjacent node coefficients by

$$B_{ijk}(x, y) = \sum_{p=i-1}^{i+2} \sum_{q=j-1}^{j+2} c_{pqk} w_{pqk}(x, y), \quad (1)$$

where c_{pqk} and $w_{pqk}(x, y)$ denote the unknown coefficient and known weight, respectively, for the node at the p th row and q th column of nodes on the k th mesh. The weights are a function only of the position on the surface patch at which the surface is being evaluated and therefore also remain fixed throughout the inversion.

Thus, the primary objective is to estimate all of the unknown node coefficients c_{ijk} , which collectively define the 3D conductivity mod-

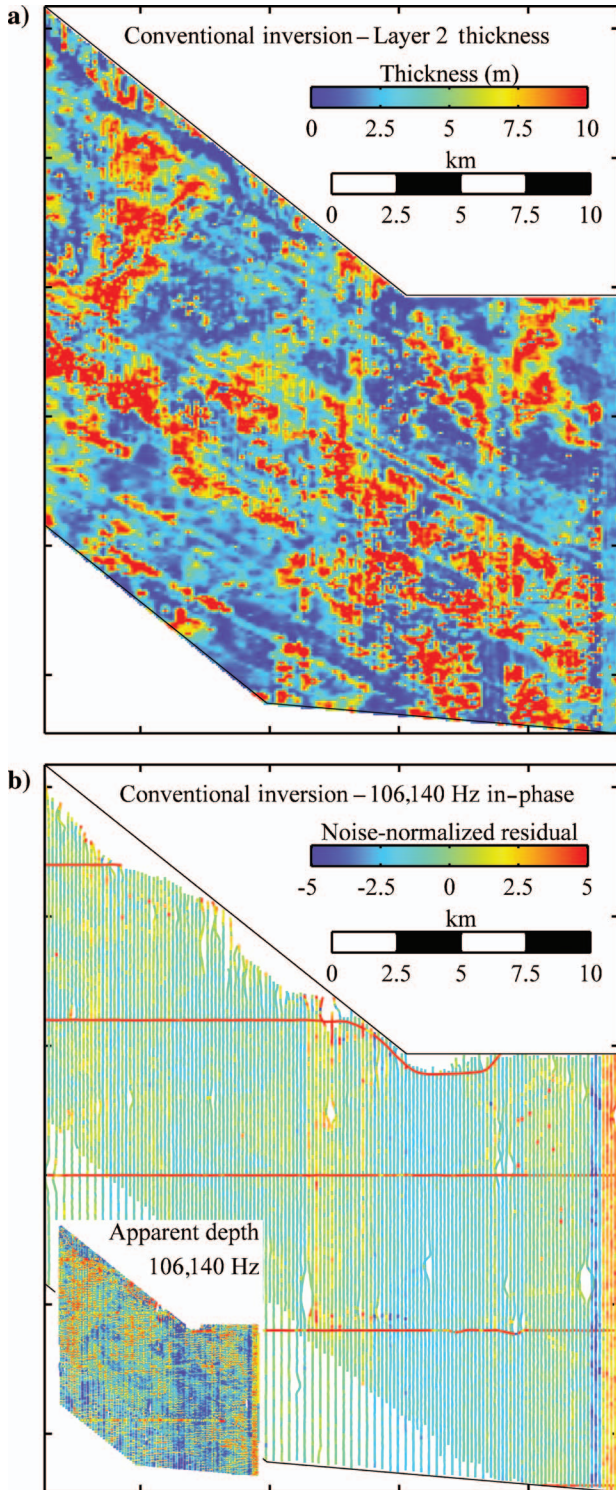


Figure 1. Results from an inversion of conventionally calibrated and processed data; (a) layer two thickness, and (b) noise-normalized 106,140-Hz in-phase residuals, with apparent depths shown inset.

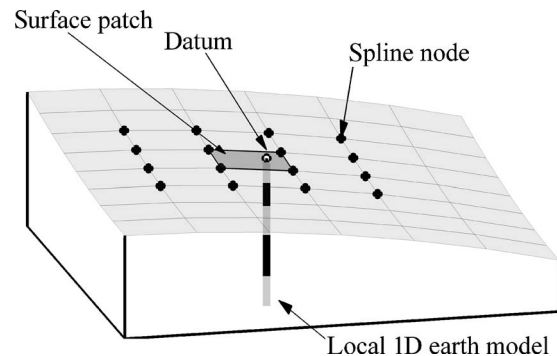


Figure 2. A schematic representation of a bicubic B-spline model and a local 1D conductivity profile.

el. There is no requirement that the spline node spacing should be equal on all meshes or that all nodes lie on a regular rectangular mesh.

Calibration model

The calibration model describes systematic calibration error in the measurement system. Calibration model parameters could be related to many conceivable sources of error. However, we consider only nonrandom sources, whose effect on the measured data can be expressed analytically. Our calibration model is based on that of Deszcz-Pan et al. (1998), which included amplitude scaling (gain); phase shift between the transmitter and receiver time reference frames (phase), and zero-level (bias) errors. We add transmitter-receiver bird altitude (height) error as another possible source of systematic calibration error.

Calibration errors could conceivably vary on the basis of survey, day, flight line, or sample acquisition entities. They may also vary on a frequency or channel basis (i.e., in-phase or quadrature data for a specific frequency). Errors may be considered constant over one such entity, or over a group of entities; alternatively, they could be considered to vary in a predictable manner (e.g., piecewise linearly or polynomially) over one entity. The specific choice of how to parameterize calibration errors is necessarily governed by the survey procedure and the characteristics of the specific system under consideration. It is also guided by a trade-off between adequate representation of the systematic calibration error, inversion stability, and size. The number of possible ways to parameterize the calibration model is large, but the best results will be achieved when the parameterization accurately describes the characteristics of the actual calibration error.

To illustrate some possibilities in the examples discussed later, we have parameterized the gain calibration errors to be different for each frequency but constant for an entire survey. We have parameterized phase to be different for each frequency, as well as different for each day of flying, to reflect the possibility of different phase errors resulting from different daily calibrations. The in-phase and quadrature bias for each frequency is deemed to be a quantity that varies piecewise linearly over the duration of each flight. We achieve this by specifying a set of fiducials that remain fixed throughout the inversion and solve for the bias value at the first fixed fiducial and the gradients between them thereafter. In this paper, height errors are regarded as level shifts over entire surveys. For most configurations, they will be the same for each frequency, at least when bird attitude is not accounted for, in which case only one height parameter is required per survey.

Observed data

The three types of observed data comprise what we call the airborne data (d_o^{air}), geoelectric data (d_o^{geo}), and interface-depth data (d_o^{int}). For airborne data, we used raw in-phase and quadrature data (i.e., before zero-level, gain, phase, or additional bias corrections have been applied). In many FDEM systems, each channel is zeroed immediately after the high-altitude zero-level observations are made. This practice introduces instantaneous level shifts in the recorded data that must be reversed before applying the style of bias parameterization discussed earlier. We included tie-line and daily repeat-line data without any special treatment (so long as they have been acquired in the same manner). Daily repeat-line data are in-

cluded because they are likely to provide good constraints on calibration parameters that vary with periods of a day or longer.

We shall call a specific depth range at a specific location a geoelectric depth interval. Then, a geoelectrical datum is the natural logarithm of the average conductivity over a particular geoelectric depth interval. Geoelectric data may be inferred from independent ground or subsurface measurements, such as borehole conductivity logs, ground-based electromagnetic surveys, and laboratory sample analysis.

Interface-depth data may include any information available regarding the depth at a specific location or to a specific interface in the layered conductivity model. These could, for example, include the depths to the standing water level observed in boreholes, as used by Brodie et al. (2004b), or the depth to basement information.

The forward problem and inversion derivatives

Our use of a layered and laterally continuous 3D conductivity model allows us to exploit the spatial coherency in the data. However, because full 3D electromagnetic modeling is computationally expensive, we use the more efficient 1D assumption in the forward problem. Prediction of a datum from the model parameters is a two-stage process. First, a local 1D conductivity profile and a set of local calibration values are computed from the model parameters. Then, the local 1D conductivity profile and local calibration values are used as input into the forward-model algorithm.

A local 1D conductivity profile, shown schematically by the banded column on Figure 2, is just the vertical conductivity-thickness structure at the datum location. It is denoted $(\boldsymbol{\sigma}, \mathbf{t})$ and is completely defined by the layer conductivities, $\boldsymbol{\sigma} = (\sigma_1, \sigma_2, \dots, \sigma_N)$, and thicknesses, $\mathbf{t} = (t_1, t_2, \dots, t_{N-1})$, which are attained from equation 1 for each spline mesh. The partial derivatives of the spline surface values (equation 1) with respect to the node coefficients are given by

$$\frac{\partial B_{ijk}}{\partial c_{pqr}} = \begin{cases} w_{pqr}; & i-1 \leq p \leq i+2, j-1 \leq q \leq j+2, k=r. \\ 0; & \text{otherwise} \end{cases} \quad (2)$$

For an airborne datum, the set of local calibration values that pertain to the datum (i.e., a specific survey, day, flight line, fiducial, and channel) must be determined. Such a set comprises gain g , phase θ , in-phase and quadrature bias b^{ip}, b^q , and height error Δh values. The set is constructed by identifying all calibration model parameters that influence the specific airborne datum, then computing the local value from the calibration model. In some cases, such as our parameterization of gain phase and height discussed earlier, a local calibration value is equivalent to one specific inversion parameter. In these cases, the local calibration value is just selected from a lookup table and the partial derivative will be unity. However, in our piecewise linear parameterization of bias, two or more inversion parameters influence a local bias calibration value. Under this scheme, the bias b' at fiducial f' that lies on the i th linear segment is

$$b' = b_1 + \left(\sum_{p=1}^{i-1} m_p (f_{p+1} - f_p) \right) + m_i (f' - f_i). \quad (3)$$

Here, b_1 is the bias at the first fixed fiducial, f_i is the i th fixed fiducial, and m_i represents the bias gradient between the i th and $(i+1)$ th fixed fiducials. The partial derivative $\partial b' / \partial b_1 = 1$ and, with respect to the gradient, is

$$\frac{\partial b'}{\partial m_k} = \begin{cases} f_{i+1} - f_i; & k < i \\ f' - f_i; & k = i \\ 0; & k > i \end{cases} . \quad (4)$$

To predict the airborne in-phase (d_p^{ip}) and quadrature (d_p^q) data, we input the local 1D conductivity profile (σ, \mathbf{t}), the local height calibration value Δh , and the altimeter measured transmitter-receiver bird height h into a 1D layered-earth, forward-modeling routine. The routine, denoted by the complex function

$$\mathbf{s}(\sigma, \mathbf{t}, h + \Delta h) = s^{ip} + js^q, \quad (5)$$

computes the theoretical in-phase s^{ip} and quadrature s^q responses where $j = \sqrt{-1}$. Our implementation of equation 5 is based upon the formulation of Wait (1982) for vertical and horizontal magnetic dipole sources above a horizontally layered medium. We assume the contribution from displacement currents is negligible and that we are dealing with magnetically nonsusceptible layers. For computation of Wait's coefficient R_0 , we take advantage of the propagation matrix method (Farquharson et al., 2004) because it is computationally efficient when the partial derivative of the airborne response with respect to several layer conductivities and thicknesses is required. The partial derivatives for the i th layer, $\partial \mathbf{s} / \partial \sigma_i$ and $\partial \mathbf{s} / \partial t_i$, as well as $\partial \mathbf{s} / \partial \Delta h$ can all be derived analytically and are omitted for brevity.

Using the remaining local calibration values (g, θ, b^{ip} , and b^q), the theoretical system responses (s^{ip} and s^q) are transformed to uncalibrated system responses (i.e., the predicted airborne data) via the calibration model equations

$$d_p^{ip} = g[(s^{ip} + b^{ip})\cos \theta - (s^q + b^q)\sin \theta] \quad (6)$$

and

$$d_p^q = g[(s^{ip} + b^{ip})\sin \theta + (s^q + b^q)\cos \theta]. \quad (7)$$

The partial derivatives of d_p^{ip} and d_p^q with respect to g, θ, b^{ip} , and b^q are straightforward to derive from differentiation of equations 6 and 7.

A predicted geoelectric datum (d_p^{geo}) is the natural logarithm of the average conductivity $\bar{\sigma}$ over the corresponding geoelectric depth interval. If this geoelectric depth interval begins in the q th layer and extends down to the r th layer and has a total length L , it can be subdivided into intervals of length l_k corresponding to its overlap with the k th layer. (If the top of a geoelectric interval coincides with the bottom interface of the q th layer, then it is said to start in the q th layer.) With this definition, the required partial derivatives are

$$\frac{\partial d_p^{\text{geo}}}{\partial \sigma_k} = \frac{l_k}{\bar{\sigma}L} \quad (8)$$

and

$$\frac{\partial d_p^{\text{geo}}}{\partial t_k} = \begin{cases} (\sigma_q - \sigma_r) / \bar{\sigma}L; & k < q \\ (\sigma_k - \sigma_r) / \bar{\sigma}L; & q \leq k < r \\ 0; & k \geq r \end{cases} . \quad (9)$$

A predicted interface-depth datum d_p^{int} is the cumulative thickness of all layers above the specified interface. The partial derivatives of d_p^{int} , with respect to the thickness of layers, are unity for layers above the interface and zero for those below. The partial derivatives of d_p^{int} with respect to all layer conductivities are zero.

Inversion scheme

The inversion minimizes an objective function of the form

$$\Phi = \Phi_d + \lambda_r \Phi_r + \lambda_x \Phi_x + \lambda_y \Phi_y + \lambda_z \Phi_z + \lambda_b \Phi_b, \quad (10)$$

where Φ_d is a data misfit term; Φ_r is a reference-model misfit term; Φ_x, Φ_y , and Φ_z are east-west, north-south, and vertical model roughness terms, respectively; and Φ_b is a bias roughness term. The λ s are multipliers that weight the relative importance of each of the terms. The data misfit Φ_d is defined in the usual error-weighted sense,

$$\Phi_d = [\mathbf{d}_o - \mathbf{g}(\mathbf{m})]^T \mathbf{C}_d^{-1} [\mathbf{d}_o - \mathbf{g}(\mathbf{m})], \quad (11)$$

where $\mathbf{d}_o = (\mathbf{d}_o^{\text{air}}, \mathbf{d}_o^{\text{geo}}, \mathbf{d}_o^{\text{int}})$ is the vector of observed data and $\mathbf{m} = (\mathbf{m}^{\text{cal}}, \mathbf{m}^{\text{ear}})$ is the vector of unknown model parameters to be estimated. The vector function $\mathbf{g}(\mathbf{m}) = \mathbf{d}_p = (\mathbf{d}_p^{\text{air}}, \mathbf{d}_p^{\text{geo}}, \mathbf{d}_p^{\text{int}})$ is the nonlinear forward model that maps the model parameters to predictions of data, and the data covariance matrix \mathbf{C}_d expresses the estimated error in the observations.

It is both convenient and intuitive to specify a reference model and quantify model roughness in terms of real physical properties rather than directly with abstract quantities like spline node coefficients. To facilitate, this we introduce the linear operator matrix \mathbf{S} that maps the model parameters \mathbf{m} to a vector of real physical properties \mathbf{r} such that $\mathbf{S}\mathbf{m} = \mathbf{r}$. The matrix \mathbf{S} is sparse and known by definition of the relationship between the model parameters and real physical properties. If we have available a reference vector \mathbf{r}_0 specified in real physical properties, then an appropriate reference model misfit term is

$$\Phi_r = [\mathbf{r}_0 - \mathbf{S}\mathbf{m}]^T \mathbf{C}_r^{-1} [\mathbf{r}_0 - \mathbf{S}\mathbf{m}], \quad (12)$$

where \mathbf{C}_r is the reference vector covariance matrix that expresses the estimated error in the reference vector.

The roughness in the east-west direction is defined as

$$\Phi_x = \mathbf{m}^T \mathbf{S}^T \mathbf{L}_x^T \mathbf{L}_x \mathbf{S} \mathbf{m}. \quad (13)$$

Analogous expressions are used for both Φ_y and Φ_z . The matrices $\mathbf{L}_x, \mathbf{L}_y$, and \mathbf{L}_z are linear second finite-difference operator matrices that operate on the logarithms of layer conductivities and thicknesses at spatially adjacent spline-mesh intersections in each direction (Constable et al., 1987). We have observed from zero levels recorded at high altitude (after instantaneous level shifts are reversed) that they vary smoothly with time over the duration of a flight. We take advantage of this by including an additional regularization term that quantifies the roughness of the bias, defined as

$$\Phi_b = \mathbf{m}^T \mathbf{L}_b^T \mathbf{L}_b \mathbf{m}. \quad (14)$$

The matrix \mathbf{L}_b is a first finite-difference operator that operates on temporally adjacent bias gradients of a given channel. We expect gain and phase calibration errors to be largely related to the on-ground location at which they were calibrated, mispositioning of calibration instruments, and human error (Fitterman, 1998). Because such errors are likely to be independent from day to day rather than smoothly varying, we have no motivation for penalizing their roughness in the parameterization scheme we have used. Our parameterization of height calibration values yields only one parameter, so regularization is not relevant in this case. If, for instance, we were to solve for a height calibration value at each airborne sample, an along-line roughness penalty term would then be appropriate.

To estimate the model parameters, we use a linearized, gradient-based iterative scheme. To begin, we make an initial estimate of the

model parameters \mathbf{m}_0 by solving the linear system $\mathbf{S}\mathbf{m}_0 = \mathbf{r}_0$, recalling that \mathbf{r}_0 is a known reference vector. At the $(n + 1)$ th iteration, the current model estimate \mathbf{m}_n is perturbed by a small amount to arrive at a new estimate, \mathbf{m}_{n+1} . In the usual way, we make use of the two-term Taylor Series expansion, $\mathbf{g}(\mathbf{m}_{n+1}) \cong \mathbf{g}(\mathbf{m}_n) + \mathbf{G}_n(\mathbf{m}_{n+1} - \mathbf{m}_n)$, where \mathbf{G}_n is the Jacobian matrix whose i, j th element is the partial derivative of the i th datum with respect to the j th model parameter evaluated at \mathbf{m}_n in model space. Then, to arrive at the new estimate, we differentiate equation 10 with respect to \mathbf{m}_{n+1} , assign the result to zero, and rearrange the terms to find that

$$\begin{aligned} & [\mathbf{G}_n^T \mathbf{C}_d^{-1} \mathbf{G}_n + \lambda_r \mathbf{S}^T \mathbf{C}_r^{-1} \mathbf{S} + \lambda_x \mathbf{S}^T \mathbf{L}_x^T \mathbf{L}_x \mathbf{S} + \lambda_y \mathbf{S}^T \mathbf{L}_y^T \mathbf{L}_y \mathbf{S} \\ & + \lambda_z \mathbf{S}^T \mathbf{L}_z^T \mathbf{L}_z \mathbf{S} + \lambda_b \mathbf{L}_b^T \mathbf{L}_b] \mathbf{m}_{n+1} \\ & = \mathbf{G}_n^T \mathbf{C}_d^{-1} [\mathbf{d} - \mathbf{g}(\mathbf{m}_n) + \mathbf{G}_n \mathbf{m}_n] + \lambda_r \mathbf{S}^T \mathbf{C}_r^{-1} \mathbf{r}_0. \end{aligned} \quad (15)$$

Equation 15 is in the familiar form of a system of linear equations, $\mathbf{A}\mathbf{m}_{n+1} = \mathbf{b}$, which can be solved to yield the required vector \mathbf{m}_{n+1} using one of several possible methods. Each datum is influenced by only the 16 adjacent spline nodes on each mesh, so the vast majority

of the entries in the matrices \mathbf{G} and \mathbf{S} are zero. The square, symmetric matrix \mathbf{A} is thus sparse. Presently, we solve the system via the conjugate gradient method using the algorithm CG described by Barrett et al. (1994) and implemented via the package IML++ described by Dongarra et al. (1994). Importantly, the matrix \mathbf{A} is never actually explicitly formed in computer memory. In dealing with its component sparse matrices, we are able to take advantage of the efficient sparse matrix algebra and storage package SparseLib++, described by Dongarra et al. (1994).

Once \mathbf{m}_{n+1} is generated, we compute a new value for Φ_d . If this value actually increases from the previous iteration, we successively reduce the length of the model perturbation by 25% and recompute Φ_d until it decreases. Then, if the new Φ_d is less than a specified target value or has decreased by less than a specified percentage since the previous iteration, the inversion is terminated and \mathbf{m}_{n+1} becomes the final solution. Otherwise, the inversion proceeds to the next iteration.

RESULTS

Synthetic data example

A 10×10 -km subset of the Riverland survey data set (discussed earlier), comprising 10 days of flying, 14 flights, 67 survey lines, and 1 tie line, were used to construct the synthetic data set. The area included five boreholes from which downhole conductivity logs were available. A single-layer conductivity model, which varied horizontally but not vertically, was synthesized from cosine functions (Figure 3a). At actual airborne sample locations, local 1D conductivity profiles were extracted and forward modeled using equation 5 to generate theoretical airborne responses for the RESOLVE system at a bird height equal to the altimeter-measured bird height plus a synthetic survey-wide height calibration error of one meter. The theoretical responses were then transformed via the calibration model equations 6 and 7 to produce synthetic, uncalibrated responses. The local calibration values used in this transformation were selected according to the parameters of the synthetic calibration model.

The gain, phase, and bias of the synthetic calibration model were parameterized as specified in the Calibration Model subsection. The six gain parameters (1.04, 0.96, 0.90, 0.86, 0.77, and 0.81, one for each of the six frequencies) were chosen to be equivalent to (i.e., the reciprocal of) the scaling factors derived for the Riverland data by the regression analysis of Brodie et al. (2004a).

The 60 phase parameters (daily phase adjustment over the ten days of flying for each of the six frequencies) were selected from a Gaussian random distribution with mean 0.0° and standard deviation 2.0° . The in-phase and quadrature bias values were taken to be linear interpolations of the zero levels observed at high altitude during the actual data acquisition. Gaussian random noise computed from the noise model derived for the RESOLVE system by Green and Lane (2003) was then added to the responses.

At each of the five borehole locations, local 1D conductivity profiles were extracted from the synthetic conductivity model to generate synthetic downhole conductivity logs. The synthetic logs were contaminated with 5% Gaussian random noise. Synthetic interface-depth data were not applicable in this single-layer example.

The synthetic data were inverted to estimate the 4620 spline node-coefficients of the single 150×150 m node-spacing mesh that represented the conductivity parameters and the 787 calibration parameters. The calibration parameters were comprised of: 6 gain parameters, 60 phase parameters, 168 beginning-of-the-flight bias param-

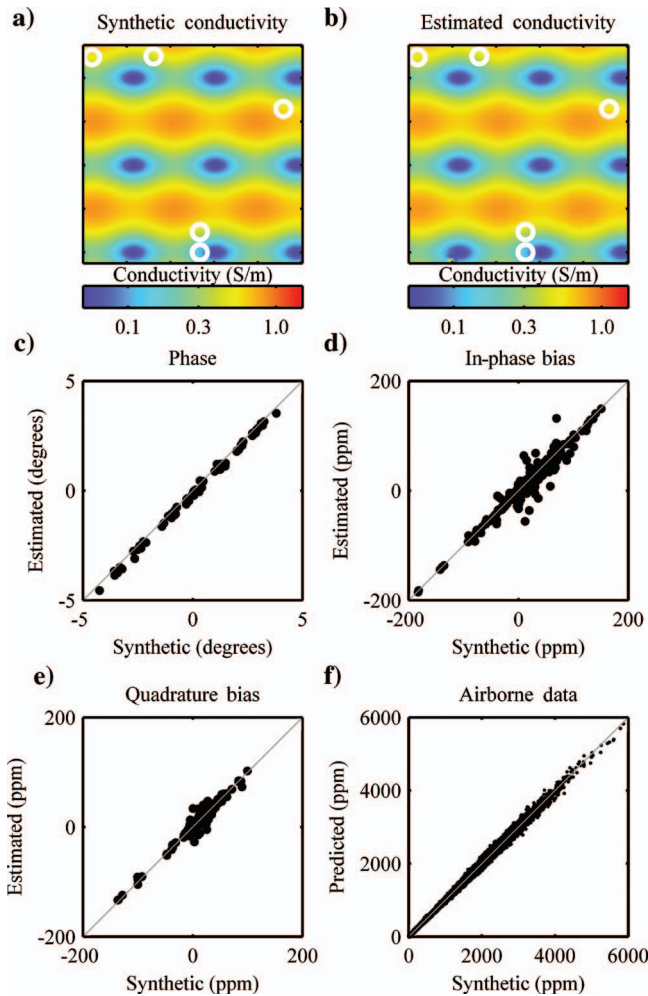


Figure 3. Holistic inversion of the synthetic data: (a) synthetic conductivity, and (b) estimated conductivity; and synthetic versus estimated; (c) phase; (d) in-phase bias; and (e) quadrature bias; and (f) synthetic versus predicted airborne data. The circles on (a) and (b) represent the location of the five synthetic boreholes.

ters, 552 bias drift rate parameters, and 1 height parameter. We used a 0.35-S/m half-space reference model, chosen to be the average of all the synthetic downhole conductivity logs. The reference value for the gain parameters was unity and the reference values for phase, bias, and height parameters were all zero.

The results of the inversion are summarized in Figure 3. Comparison of Figure 3a with Figure 3b shows that the conductivity has essentially been estimated perfectly. The scatter plots (Figure 3c–e) show that the inversion has estimated the calibration parameter values well, as the points are clustered about the diagonal, which represents perfect estimation. For brevity, we have not shown the height and gain scatter plots here, but all these points lie on the diagonal. If Gaussian noise is not included in the synthetic data, all of the parameters are estimated exactly. This indicates that the scatter of points about the diagonal in Figure 3 is caused by the presence of noise. It suggests that, at least in this case where the parameterization of the conductivity and calibration models is consistent with the synthetic models and with a suitable choice of λ s, there is no fundamental trade-off between the five classes of parameters. However, for real data sets, we recognize that because of nonuniqueness and noise, one could conceive of scenarios where there would be fundamental trade-offs between parameters. Figure 3f shows that the predicted airborne data are consistent with the estimated model parameters. The geoelectric data, not shown here, are also fitted exactly.

Real survey data example

The subset of the Riverland Survey that we have chosen for the real example covers one-quarter (406 km²) of the total survey area. It is the largest portion that we are currently able to invert on a stand-alone computer with two gigabytes of physical memory, and using the data subsampling and conductivity model specifications described below. The airborne data were subsampled to every seventeenth sample (~ 50 m) along flight lines. The subset area is traversed by 2590 line kilometers of survey data. These data range over 15 days of flying, 27 flights, and 171 flight lines, four of which are tie lines and 19 of which are daily repeat lines. Brodie et al. (2004b) give relevant background on the geological setting and report on the conventional sample-by-sample inversion of the data. Their five-layer conceptual model is shown in Figure 4.

The purpose of the survey was to map the distribution and thickness of the Blanchetown Clay. Therefore, a variable conductivity and thickness formulation, in which the clay layer was represented by the second layer, was preferred over the potentially more stable fixed-thickness and vertically smooth style of formulation (e.g., Farquharson et al., 2004). Brodie et al. (2004b) generate a smoothly varying water-table elevation surface using information from boreholes. This was converted to water-table depths and then included as interface-depth data to constrain the cumulative thickness of the top three layers in the inversion. Similarly, groundwater conductivity data from boreholes were used to create a groundwater conductivity surface. This was converted to bulk conductivity below the water table via an empirical relationship and was then used as a spatially varying reference-model value for the conductivity of layers 4 and 5. Downhole conductivity logs and driller's lithological logs were used to derive the means and standard deviations required for construction of the reference vector covariance matrix. In the holistic inversion, we have used the same conceptual model and prior information.

The layer 1 thickness spline mesh was the only nonsquare mesh and had the finest resolution, at 150×75 m east-west \times north-south, allowing it to accommodate the relatively rough surface topography influenced by east-west-orientated sand dunes. Other meshes had 150-m node spacing in both directions, except for the layer 4 conductivity mesh, which had a node spacing of 300 m and the layer 4 thickness and layer 5 conductivity meshes, which had a node spacing of 1000 m. The reference conductivities of the top three layers were fixed at 0.030, 0.240, and 0.065 S/m and were spatially variable for the lower two layers as explained above. The standard deviations of the reference conductivities, in natural logarithm units, were 0.125, 0.250, 0.125, 0.625, and 0.045. The reference thickness was 3 m for the top two layers. It was spatially variable for layer 3 and based on the depth to groundwater surface, explained earlier. Layer 4 thickness was fixed at 10 m. The standard deviation of the reference thicknesses was 2.5 natural logarithm units.

There were 148,559 unknowns to be estimated in total. Of these, 146,459 were spline node coefficients and 2100 were calibration parameters. The calibration model included 6 gain and 90 (6 frequencies \times 15 days) phase parameters. We used a piecewise linear bias parameterization with the fixed fiducials chosen such that they were spaced evenly in time between the first and last samples in the flight and at intervals as close as possible to 20 minutes. This required 324 (6 frequencies \times 2 channels \times 27 flights) start-of-flight bias parameters and 1680 bias gradient parameters. In creating the reference calibration model, we assumed the data did not require calibration and used a value of unity for the gain parameters and zero for phase and bias calibration parameters.

We reversed the instantaneous level shifts that had been introduced into the data during the high-altitude zero-level procedure as shown in Figure 5. This was necessary to return the data to a state as if the system were allowed to drift normally so the piecewise linear bias parameterization could be used. Power-line and electric fence

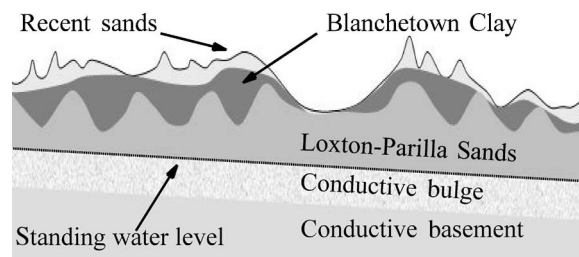


Figure 4. The conceptual model used in the inversion.

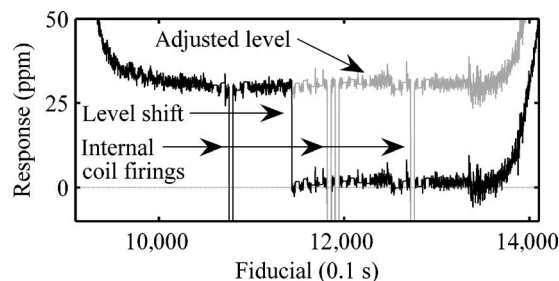


Figure 5. High-altitude 385-Hz in-phase data before (black) and after (gray) an instantaneous level shift reversal. The high values at both ends of the plot are caused by the bird being nearer to the ground (i.e., within ground effect).

filters (27 m median and hanning filters), identical to those applied in the conventional processing, were applied to the data. Aside from this preprocessing, the airborne data used in the holistic inversion were as recorded onboard the helicopter. Neither zero-level subtraction, nor any other conventional processing corrections were preapplied.

There were 47,934 airborne samples and thus 575,208 airborne data in total. The noise model of Green and Lane (2003) was used to estimate noise in the airborne data. The 17 downhole conductivity logs in the area were averaged over 2-m depth intervals that provided 330 geoelectric data points. They were assigned a noise level of 0.1 natural logarithm decades. We used the water table elevation surface to generate interface-depth data for the interface between layers 3 and 4. We chose the 113,961 interface-depth data to be located on a 60-m regular grid and assigned them a noise level of 0.2 m. The interface-depth data effectively force the cumulative thickness of the upper three layers to equal the water-table depth.

Reference model constraints were imposed. A diagonal reference vector covariance matrix C_r was used. The elements corresponding

to conductivity model parameters were selected from standard deviations of the layer conductivities and thicknesses noted earlier. For the calibration parameters, we used standard deviations of 0.1 for gain and 0.5 for phase; for bias, we used the standard deviation of the high-altitude zero-level estimates observed during the survey. Horizontal roughness constraints were also imposed. Vertical roughness constraints were not enforced because of our objective of maintaining sharp contrasts at layer interfaces. The roughness of the thickness of the topmost layer was downweighted because the presence of sand dunes meant that the top layer was not expected to be smooth at the scale of the spline-node spacing.

The estimated layer conductivities and thicknesses are shown in Figure 6. The images are free of elongate artifacts in the north-south flight-line direction and are also consistent with the conceptual model. This is a very satisfying outcome for the inversion of virtually raw airborne survey data. The layer 1 images reflect the dry and resistive sand sheets and east-west-orientated sand dunes that are observed in the Riverland area. The north-west to southeast trends that are abundant in the deeper layer images are consistent with the conceptual geological model of the Blanchetown Clay having infilled the Pliocene strandline-dominated paleo-topography. The layer 2 thickness image shows the variability in thickness of the Blanchetown Clay (the objective of the survey) and how it is influenced by the interpreted strandlines. It shows how this layer is locally dissected, or absent, because of the reworking of this material during the Quaternary. The strong narrow bands in the layer 4 conductivity image were also detected by Brodie et al. (2004b) and were interpreted as possibly caused by systematic variation of the porosity of the Loxton-Parilla Sands where they are intersected by the water table.

We noted earlier that Brodie et al. (2004a) derived scaling corrections to allow them to fit the conventionally calibrated and processed Riverland data. In Figure 7a, the reciprocal of the gain estimated from the holistic inversion is plotted against the scaling factors derived by Brodie et al. (2004a). The use of the reciprocal is required for proper comparison because their scaling factors were designed to transform acquired data to theoretical data, while our gain parameters have the reverse effect. Figure 7a shows that there is good

agreement between the two sets of gain factors, which gives us some confidence in the credibility of the estimated gains. However, this is not an independent verification of these parameters because many of the same downhole logs were used in both methods.

Figure 7b summarizes the phase parameters returned by the holistic inversion. For the 385-Hz phase parameters, an average phase of -3.68° was estimated. This compares well with the $+3.5^\circ$ phase rotation applied during conventional processing, given the reversed transformation direction discussed above. Phase rotation was applied to the 106,140-Hz data in the conventional processing ranging from $+2.0^\circ$ to -3.5° , depending on the flight number. Phase rotations were not applied to other frequencies in the conventional processing.

Figure 8 shows the correlation between the predicted bias values at the time of each set of high-altitude zero-level observations and the observed zero-levels. With the exception of the 106,140-Hz in-

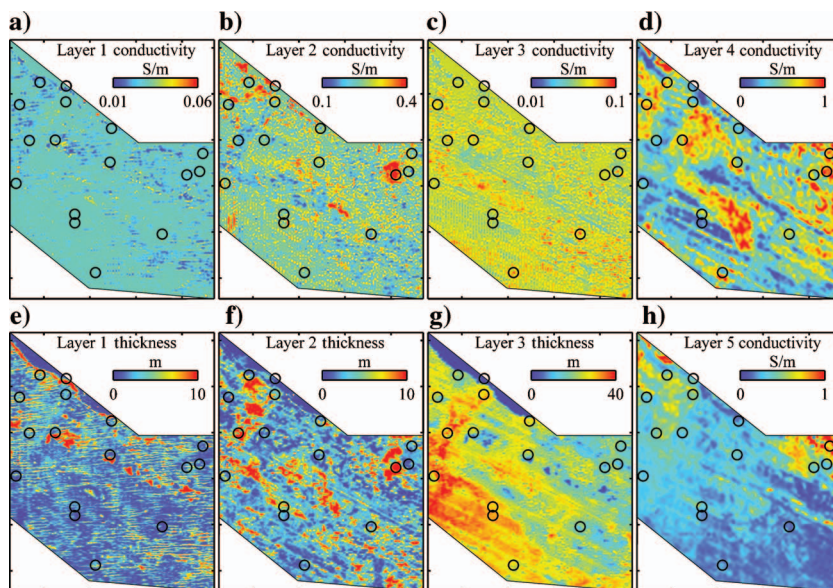


Figure 6. Layer conductivity and thickness images resulting from the holistic inversion. Circles represent the location of downhole conductivity logs used in the inversion.

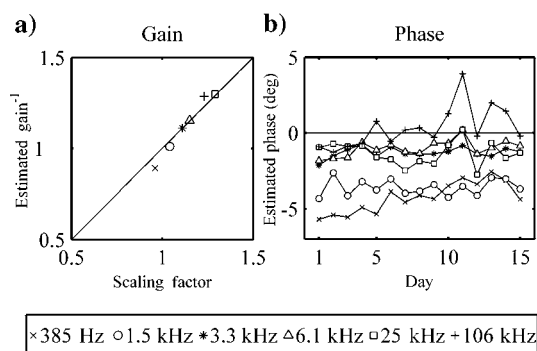


Figure 7. (a) Comparison of scaling factors derived by Brodie et al. (2004a) and gains estimated from the holistic inversion. (b) Phase parameters for each day of flying estimated from the holistic inversion.

× 385 Hz ○ 1.5 kHz * 3.3 kHz △ 6.1 kHz □ 25 kHz + 106 kHz

phase data (discussed later), there is a remarkably good correlation. Note that the observed zero levels were not used to create the reference or starting models, so the good correlations cannot be described as predestined. Where observed zero levels are available, they could be used in the inversion as additional constraints. We have not used them here to demonstrate that, under the right conditions, it may be feasible to eliminate zero-level observations altogether. This would reduce acquisition costs considerably.

Figure 9a shows the estimated layer 2 thickness from the holistic inversion. Comparing this with the conventional method (Figure 1a) illustrates the superiority of the holistic inversion method. First, the conventional results are tainted with north-south elongate anomalies that correspond to individual survey lines or flights. Second, the holistic results are less noisy and thereby better preserve continuity of many of the features, especially the northwest-southeast trends. The noise-normalized residuals from the holistic inversion of the nearly raw data (Figure 9b) are not systematically correlated with individual survey lines or flights like those in Figure 1b. This suggests that the holistic inversion is modeling the systematic calibration error ad-

equately. Furthermore, the magnitudes of the residuals in the holistic inversion are substantially smaller and more Gaussian distributed in appearance. The two notable coherent features, running at an angle to the flight lines (indicated by arrows) on Figure 9b, coincide with anomalies in the power-line and sferics monitor channels.

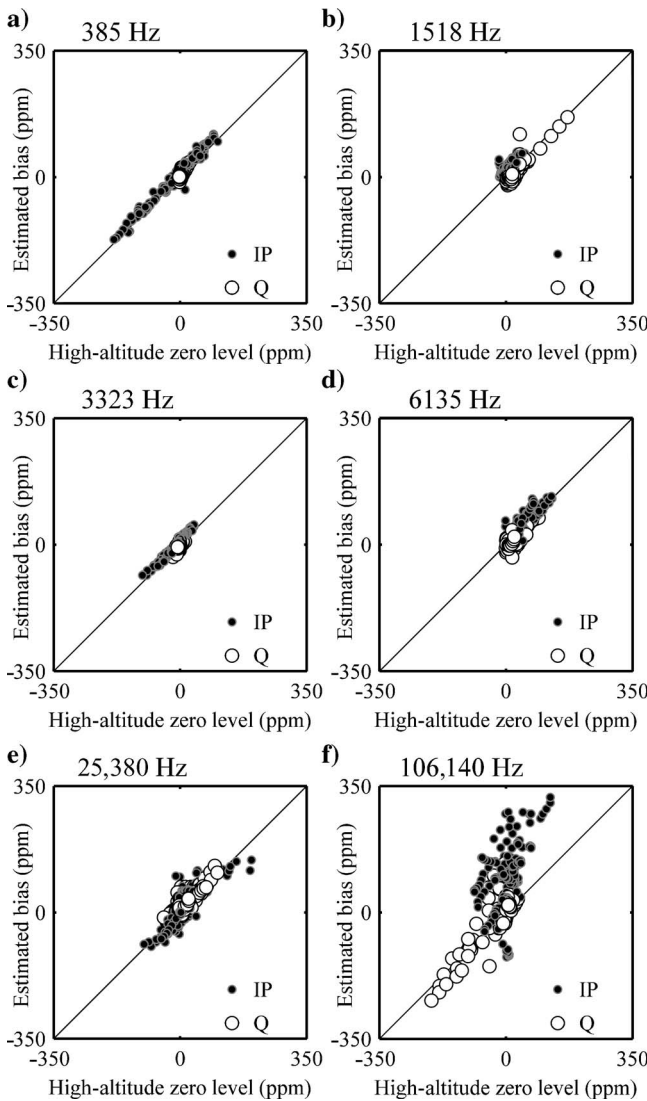


Figure 8. Zero levels observed at high altitude versus the bias estimated from the holistic calibration model.

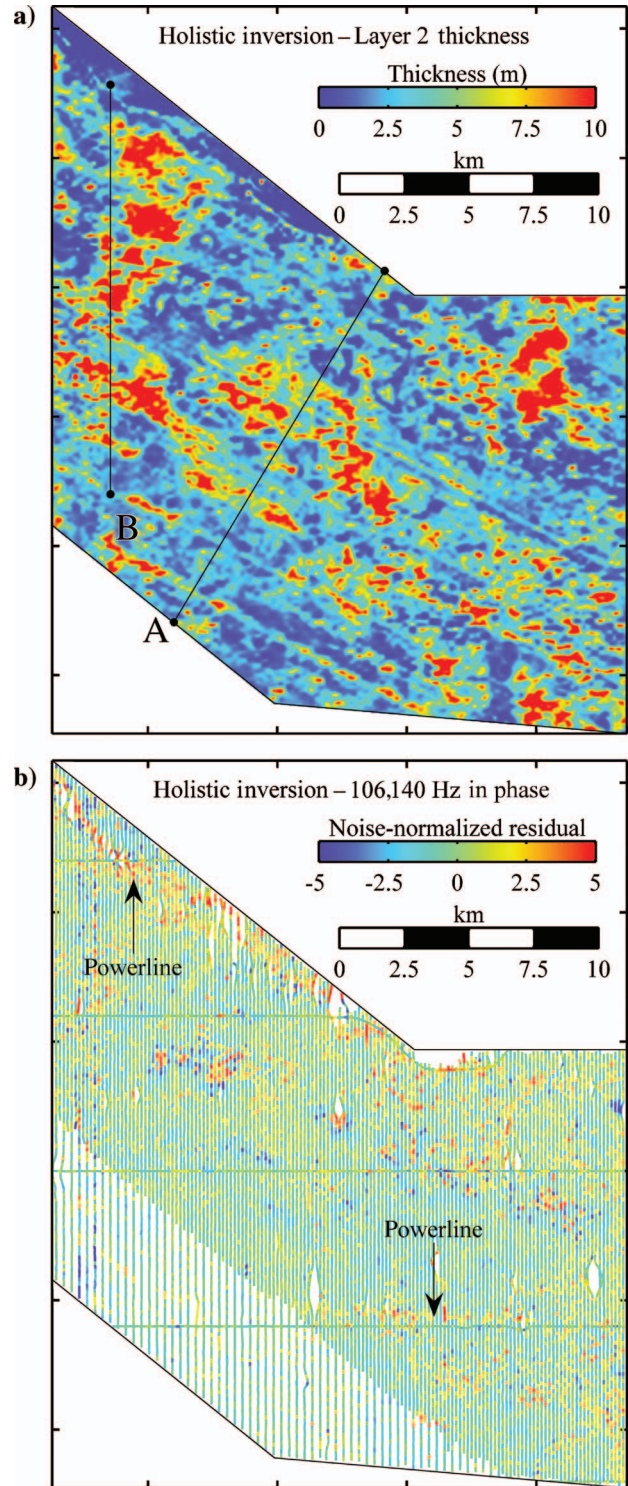


Figure 9. Results from the holistic inversion: (a) layer two thickness and (b) noise-normalized 106,140-Hz in-phase residuals. Profiles A and B show the locations of the sections in Figure 10.

We noted earlier the poor correlation between the observed and predicted 106,140-Hz in-phase zero levels (Figure 8f). Considering the improved results obtained using the new method, we suspect that the holistic inversion has provided a better estimate of bias than the observed high-altitude zero levels. However, we have no explanation as to why the observed high-altitude zero levels would be wrong, if indeed they are wrong.

Figure 10 demonstrates that conductivity sections produced from the holistic inversion are more geologically realistic than those resulting from conventional sample-by-sample inversions. In Figure 10a and b, holistic inversion sections are presented for the profiles

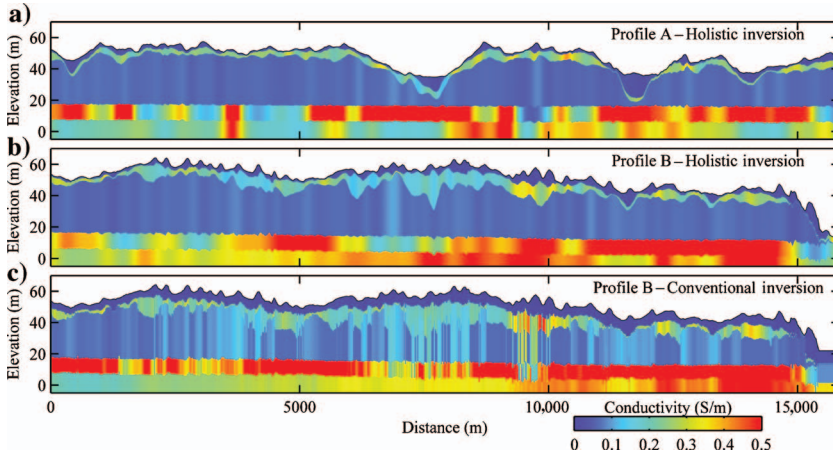


Figure 10. Conductivity sections through Profiles A and B shown on Figure 9a and Figure 11. Panels (a) and (b) show results from the holistic inversion, while (c) shows results from a conventional inversion.

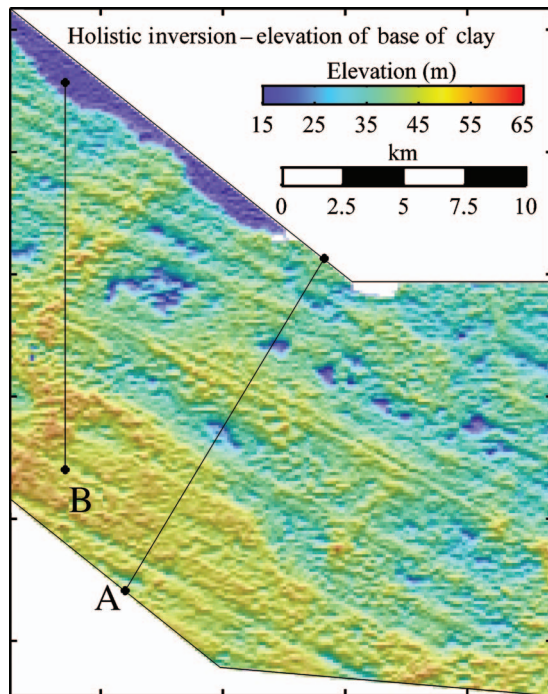


Figure 11. Holistic inversion prediction of the elevation of the base of the clay layer illuminated from the north. Profiles A and B show the locations of the sections in Figure 10.

marked A and B on Figures 9a and 11. Figure 10c is a section resulting from the conventional inversion of data along profile B. None of the three sections has been smoothed. The holistic inversion sections are more geologically realistic because they do exhibit the many lateral discontinuities apparent in the conventional inversion section. Conventional inversion results often require some degree of smoothing before being compiled into presentable sections because of such discontinuities. The discontinuities are probably caused partly by fundamental ambiguity, partly by bird-motion noise, as shown in Fitterman and Yin (2004), and short-period noise sources.

The lateral continuity imposed by the bicubic B-spline conductivity model enables the holistic inversion to fit through the short period noise, which is not possible with a sample by sample inversion. This is an advantage shared by the laterally constrained inversions of Auken et al. (2005), who also claim that the lateral constraint improves the resolution of potential equivalences. The relatively narrow bands visible in the layer 4 conductivity of the sections may not look geologically realistic at first appearance. However, it is clear from Figure 6d and h that the banding is spatially coherent.

In Figure 11 we have imaged the elevation of the interface representing the base of the clay (layer 2). Brodie et al. (2004b) interpreted this surface to represent the strandline-influenced Pliocene palaeo-topography. The spatial patterns and their geological explanation are supportive of the more subtle features shown in the holistic inversion sections. We find it rather encouraging that such geologically revealing results are able to be produced from the holistic inversion of near-survey data.

Figure 12a demonstrates the overall good fit between the observed geoelectric data (averages over each 2-m interval of 17 downhole conductivity logs) and the predicted geoelectric data computed from the holistic conductivity model. The largest discrepancies are for the datum in the lower end of the predicted conductivity range, which corresponds to intervals in the tightly constrained layers 1 and 3. Figure 12b shows the very good fit between the observed interface-depth data (groundwater depths) and the predicted interface-depth data computed from the sum of the top three layers of the holistic conductivity model.

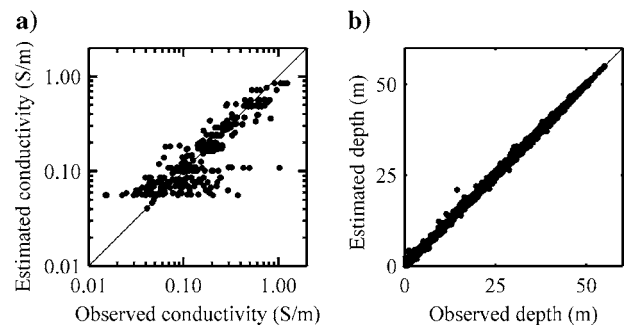


Figure 12. (a) The fit between the observed geoelectric data (from downhole conductivity logs) and predicted geoelectric data. (b) The fit between the observed (groundwater depths) and predicted (depth to the bottom of the third layer) interface-depth data.

DISCUSSION

One of our criticisms of conventional processing methods based on appraisal of apparent conductivity images was that processing decisions were subjective and required trial-and-error iterations. The holistic approach has introduced greater objectivity and reproducibility through use of a mathematical calibration model and a formal inversion procedure constrained by prior independent information. However, some subjective elements remain. The choice of the regularization parameters (λ s) in the objective function (equation 10) is manual and fixed for the entirety of the inversion. The λ s are chosen to allow convergence to an acceptable data misfit while yielding feasible calibration and conductivity models. As with most other inversion algorithms, choosing the λ s is the least repeatable and least robust part of the method and requires some experimentation by running the software several times. This situation potentially could be improved by using one of the automated methods described by Farquharson and Oldenburg (2004).

The survey data example presented involved the use of a relatively advanced conceptual conductivity model, downhole conductivity data and interface-depth data. The holistic approach can be applied in a situation where little is known about the survey area. This is the subject of current work.

We believe that a holistic approach could be successfully employed in other geophysical methods in which the knowledge of the measurement system is incomplete and multiple data streams are coupled via the common underlying geology. Time-domain electromagnetics and gamma-ray spectrometry are obvious candidates.

CONCLUSIONS

We demonstrate a method that draws together all of the available information about a problem and considers them simultaneously to produce an optimal result. Consideration of all the frequencies simultaneously has allowed the resolution of interfrequency inconsistencies. Overall, we have made the data processing more objective but have also identified potential improvements in this regard. The holistic approach ensures all airborne data and prior independent information are consistent with common conductivity and calibration models. Because it is an all-at-once approach, multistage error propagation is avoided. In this way, we have been able to extract more value from the airborne data by capitalizing on both the interfrequency and spatial-coherency information that is contained in an airborne data set but are not conventionally utilized.

Synthetic tests have shown that it is possible to accurately recover conductivity and calibration model parameters. The application to real survey data has shown that the holistic approach has produced superior inversion models. This is demonstrated by coherent and artifact-free maps in plan and section form, the spatial noncorrelation of inversion residuals, and lower overall misfit. Although conventional sequential approaches are convenient and computationally less challenging to implement than the holistic approach, the example shows that the holistic approach is tractable. It may in fact provide cost savings because it avoids the iterative, time-consuming calibration-processing-recalibration paradigm. Because we were able to obtain superior results without specific use of high-altitude zero-level observations, our results also suggest that further cost savings can be achieved by eliminating these procedures from surveys. Applications of the holistic approach to other geophysical methods are also highlighted.

ACKNOWLEDGMENTS

The Riverland data were acquired by the South Australian Salinity Mapping and Management Support Project, which is jointly funded by the Commonwealth and South Australian Governments under the National Action Plan for Salinity and Water Quality. We thank Geoscience Australia (GA) for supporting this research and Richard Lane and Brian Minty (GA) for valuable internal reviews of the draft. We also thank the reviewers, Maria Deszcz-Pan, Richard Smith, Colin Farquharson, and an anonymous associate editor for their constructive criticisms and helpful suggestions. Brodie publishes with the permission of the CEO of GA.

REFERENCES

- Auken, E., A. V. Christiansen, B. H. Jacobsen, and N. Foged, 2005, Piecewise 1-D laterally constrained inversion of resistivity data: *Geophysical Prospecting*, **53**, 497–506.
- Barrett, R., M. Berry, T. F. Chan, J. Demmel, J. Donato, J. Dongarra, V. Eijkhout, R. Pozo, C. Romine, and H. Van der Vorst, 1994, *Templates for the solution of linear systems: Building blocks for iterative methods*: SIAM Press.
- Bartels, R. H., J. C. Beatty, and B. A. Barsky, 1987, *An introduction to splines for use in computer graphics and geometric modeling*: Morgan Kaufmann.
- Brodie, R. C., A. A. Green, and T. J. Munday, 2004a, Calibration of RESOLVE airborne electromagnetic data — Riverland and East Tintinara, South Australia: Cooperative Research Centre for Landscapes, Environment and Mineral Exploration Open File Report 173, accessed March 13, 2006, <<http://crclme.org.au/Pubs/OFR171-180/OFR173.pdf>>.
- , 2004b, Constrained inversion of RESOLVE electromagnetic data — Riverland, South Australia: Cooperative Research Centre for Landscapes, Environment and Mineral Exploration Open File Report 175, accessed March 13, 2006, <<http://crclme.org.au/Pubs/OFR171-180/OFR175.pdf>>.
- Brodie, R., and M. Sambridge, 2004, Holistically calibrating, processing and inverting frequency-domain AEM surveys: *Preview*, **111**, 100.
- Constable, S. C., R. L. Parker, and C. G. Constable, 1987, Occam's inversion: A practical algorithm for generating smooth models from electromagnetic sounding data: *Geophysics*, **52**, 289–300.
- Deszcz-Pan, M., D. V. Fitterman, and V. F. Labson, 1998, Reduction of inversion errors in helicopter EM data using auxiliary information: *Exploration Geophysics*, **29**, 142–146.
- Dongarra, J., A. Lumsdaine, R. Pozo, and K. A. Remington, 1994, A sparse matrix library in C++ for high performance architectures: Proceedings of the Second Object Oriented Numerics Conference, 214–218.
- Farquharson, C. G., and D. W. Oldenburg, 2004, A comparison of automatic techniques for estimating the regularization parameter in non-linear inverse problems: *Geophysical Journal International*, **156**, 411–425.
- Farquharson, C. G., D. W. Oldenburg, and P. S. Routh, 2004, Simultaneous 1D inversion of loop-loop electromagnetic data for magnetic susceptibility and electrical conductivity: *Geophysics*, **68**, 1857–1869.
- Fitterman, D. V., 1998, Sources of calibration errors in helicopter EM data: *Exploration Geophysics*, **29**, 65–70.
- Fitterman, D. V., and C. Yin, 2004, Effect of bird maneuver on frequency-domain helicopter EM response, *Geophysics*, **69**, 1203–1215.
- Fraser, D. C., 1978, Resistivity mapping with an airborne multicoil electromagnetic system: *Geophysics*, **43**, 144–172.
- Green, A., 2003, Correcting drift errors in HEM data: *Preview*, **102**, 84.
- Green, A., and R. Lane, 2003, Estimating noise levels in AEM data: *Preview*, **102**, 70.
- Gyulai, A., and T. Ormos, 1999, A new procedure for the interpretation of VES data; 1.5-D simultaneous inversion method: *Journal of Applied Geophysics*, **41**, 1–17.
- Hodges, G., 2002, Technological advantages of the RESOLVE HEM system: accessed October 8, 2004, <http://www.fugroairborne.com.au/Resources/tn/resolve_adv.shtml>.
- Huang, H., and D. C. Fraser, 1999, Airborne resistivity data leveling: *Geophysics*, **64**, 378–385.
- , 2003, Inversion of helicopter electromagnetic data to a magnetic conductive layered earth: *Geophysics*, **68**, 1211–1223.
- Ley-Cooper, Y., and J. Macnae, 2004, Model-consistent rescaling to correct amplitude calibration problems in HEM data: *Exploration Geophysics*, **35**, 277–282.

Liu, G., and A. Becker, 1990, Two-dimensional mapping of sea-ice keels with airborne electromagnetics: *Geophysics*, **55**, 239–248.

Sasaki, S., 2004, Inversion of airborne EM data accounting for terrain and inaccurate flight height: 74th Annual International Meeting, SEG, Expanded

Abstracts, 648–651.

Valleau, N. C., 2000, HEM data processing—A practical overview: *Exploration Geophysics*, **31**, 584–594.

Wait, J. R., 1982, *Geo-electromagnetism*: Academic Press Inc.